Ploughing friction on wet and dry sand

Liefferink, R.W.; Weber, B.A.; Bonn, D.

Published in:
Physical Review E

DOI:
10.1103/PhysRevE.98.052903

Ploughing friction on wet and dry sand

R. W. Liefferink,[1] B. Weber,[1,2] and D. Bonn[1]
[1]*Institute of Physics, University of Amsterdam, Science Park 904, 1098 XH Amsterdam, Netherlands*
[2]*Advanced Research Center for Nanolithography, Science Park 110, 1098 XG Amsterdam, Netherlands*

(Received 27 August 2018; published 6 November 2018)

The friction for sliding objects over partially water-saturated granular materials is investigated as a function of the water volume fraction. We find that ploughing friction is the main sliding mechanism: The slider leaves a deep trace in the sand after its passage. In line with previous research and everyday experience, we find that the friction force varies nonmonotonically with the water volume fraction. The addition of a small amount of water makes the friction force sharply drop, whereas too much added water causes the friction force to increase again. We present a ploughing model that quantitatively reproduces the nonmonotonic variation of the friction force as a function of water volume fraction without adjustable parameters. In this model, the yield stress of the water-sand mixture controls the depth to which the hemisphere sinks into the sand and the force that is required to plough through the water-sand mixture. We show that the model can also be used for other ploughing friction experiments, such as an ice skate that leaves a ploughing track on ice.

DOI: 10.1103/PhysRevE.98.052903

I. INTRODUCTION

The mechanics of sliding over or digging in soil is crucial to many natural phenomena such as plant root growth [1–3], terradynamics [4], and antlion hunting strategies [5,6]. Industrially, very similar phenomena control processes in agriculture [7], the production of pharmaceuticals [8], or soil transport through pipes [9]: The importance of the manipulation of granular materials is difficult to overestimate since more than 10% of the world energy consumption is spent on it [10]. In all of the above phenomena and processes, the mechanics of granular materials is greatly impacted by the presence of small amounts of water. When water is introduced to a granular system, liquid bridges form between neighboring grains and bind them together, resulting in a cohesive material [11–16]. The stiffness of a granular material, quantified, for instance, by the elastic shear modulus G', varies nonmonotonically with the addition of liquid [17]. The stiffness is optimal when small liquid bridges form between the grains, which results in attractive forces binding the granular material together. At higher water contents, the capillary bridges start to coalesce, thereby decreasing the shear modulus. This intricate interplay between mechanical strength and water content can be illustrated by building sandcastles with sand that has been wetted with a varying amount of water: The highest sandcastle is constructed by mixing the sand with some (but not too much) water [18]. Remarkably, sliding friction on water-sand mixtures follows very similar (nonmonotonic) behavior in which the addition of a few percent of water can greatly reduce the friction while too much water makes the sand muddy and difficult to slide over [19]. Arguably, the ancient Egyptians, who transported statues and pyramid blocks per sledge through the desert, were aware of this as their tomb drawings show a person pouring water onto the ground in front of their sledge [20,21]. It therefore appears that the nontrivial relation between sliding friction on a granular material and water content of a granular material has been exploited for thousands of years. It was previously shown that the sliding friction on wetted sand correlates with the shear modulus of the water-sand mixture: The friction coefficient decreases roughly linearly with the increase in shear modulus [19]. In this paper we present sphere-on-sand sliding experiments and show that the relation between the friction force and stiffness is fully described by a ploughing model that takes advantage of the simple sphere-on-flat geometry.

II. EXPERIMENT

In the sliding experiments, we use a tensile tester to horizontally pull a smooth stainless steel hemisphere of radius $R = 52.5$ mm over a water-sand mixture. Dry sand is mixed with demineralized water and compacted by repeated tapping. The normal force is controlled by filling the hemisphere with dead weights. The tensile tester measures the pull force while imposing a constant slow sliding speed of 4 mm/s over a total sliding distance of 130 mm to be in a quasistatic regime; variation of the sliding speed does not lead to an appreciable change in friction force in this regime [Fig. 1(a)]. In agreement with earlier measurements [19], we find that the friction coefficient, defined as the ratio between friction force and normal force, first decreases as more water is added to the sand and then increases again (see Fig. 2). What mechanism drives this nonmonotonic variation of the friction force with water content? In each of the sliding experiments, the hemisphere creates a clear ploughing track, the width of which can be measured after the sliding stops. Interestingly, we find that the width of the ploughing track also varies nonmonotonically with the water volume fraction, just like the friction coefficient (Fig. 3): Sliding is more difficult when the hemisphere sinks deeper into the sand.

The presence of a ploughing track indicates that during sliding, the water-sand mixture is plastically deformed in both

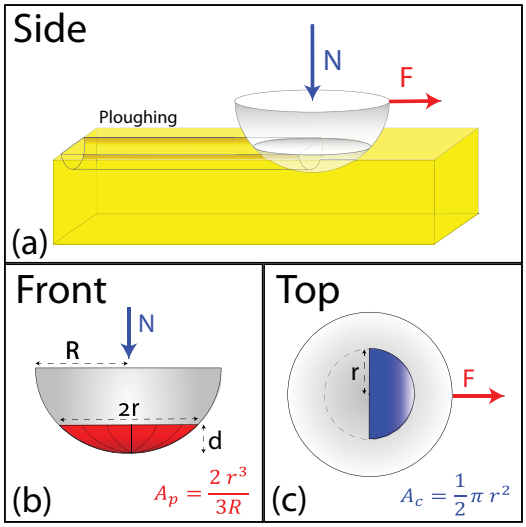

FIG. 1. Schematic representation of the ploughing experiment. (a) Side view: Normal (N) and frictional (F) forces act on the sliding hemisphere. All experiments were performed using polydisperse (100–1000 μm grains) ISO 679 standard sand, which is first dried in an oven and cooled down to room temperature. The sphere is pulled forward by a Zwick/Roell Z2.5 tensile tester, which imposes a constant displacement speed (4 mm/s) and measures the force F required with a load cell (Z6FD1, precision of 5 mN). Subsequently, the final radius r of the track drawn in the water-sand mixture perpendicular to the movement is measured. (b) Front view: the hemisphere with radius R, where the ploughing cross section A_P (red) can be calculated with use of the track radius r. The cross section can be written as $A_P \approx \frac{4}{3}rd$, with the depth of penetration $d \approx \frac{r^2}{2R}$ if $d \ll R$. Consequently, the ploughing area is $A_P = \frac{2r^3}{3R}$. Note that the assumption $d \ll R$ results in a relative error in A_P and μ [with Eq. (2)] of less than 4.5% for $r \leqslant 20$ mm ($\frac{r}{R} \leqslant 0.38$). However, for $r = 40$ mm, the relative error increases to 21%, which results in an underestimation of the friction coefficient for $\phi_w = 0\%$ in Fig. 2. (c) Top view: the hemisphere with the projected area of contact A_c (blue).

the normal and tangential directions. To quantify the stresses involved in this plastic deformation we simply divide the external forces by the area on which they act. In the normal direction the gravitational force that acts on the hemisphere is supported by the projected area of contact $A_c = \frac{1}{2}\pi r^2$ [see Fig. 1(c)], leading to an average contact pressure of $P_h = N/A_c$ which defines the penetration hardness of the water-sand mixture, P_h (Fig. 4). We find that the addition of some (but not too much) water has a dramatic effect on the penetration hardness of the compacted water-sand mixture: While dry sand can only support a stress of 3 kPa, ideally wetted sand supports up to 80 kPa of normal stress before showing a marked plastic deformation. When too much water is added to the sand, the mixture becomes muddy and the penetration hardness drops again to a value of 20 kPa at 25% water volume fraction. The nonmonotonic behavior of the penetration hardness is qualitatively similar to that of the elastic shear modulus. The physics behind the behavior of the latter is fully (and quantitatively) understood: The initial increase when small amounts of water are added is due to the formation of more and more liquid bridges between neighboring grains. The subsequent decrease at higher water content results from the filling up of the bridges: The smaller the liquid bridge, the higher the Laplace pressure holding two grains together and hence the stiffer the system; ultimately the coalescence of the liquid bridges at even higher water content leads to an even smaller modulus, as the Laplace pressure becomes very small [17]. The behavior of the modulus can be roughly approximated by first a linear increase with increasing water content; for a fixed bridge volume the number of bridges scales linearly with the amount of fluid added [17]. For the decrease of the stiffness, the coalescence of the liquid bridges is the dominant effect; we can assume that this is a random (Poisson) process, so an exponential decrease of the hardness should be observed for increasing water content. If we apply the same ideas to the penetration hardness, we get a very satisfactory description of the data, given by the solid line in Fig. 4.

The penetration hardness then controls the depth to which the hemisphere penetrates the water-sand mixture. Therefore, if the load is varied, the contact area increases until the pressure again reaches the penetration hardness. Consequently, the ploughing track increases with increasing normal force, as is shown in Fig. 5 for several water fractions. The dashed line represents the ploughing track radius based on the calculated average penetration hardness with $r(\phi_w, N) = \sqrt{\frac{N}{\frac{1}{2}\pi P_h(\phi_w)}}$.

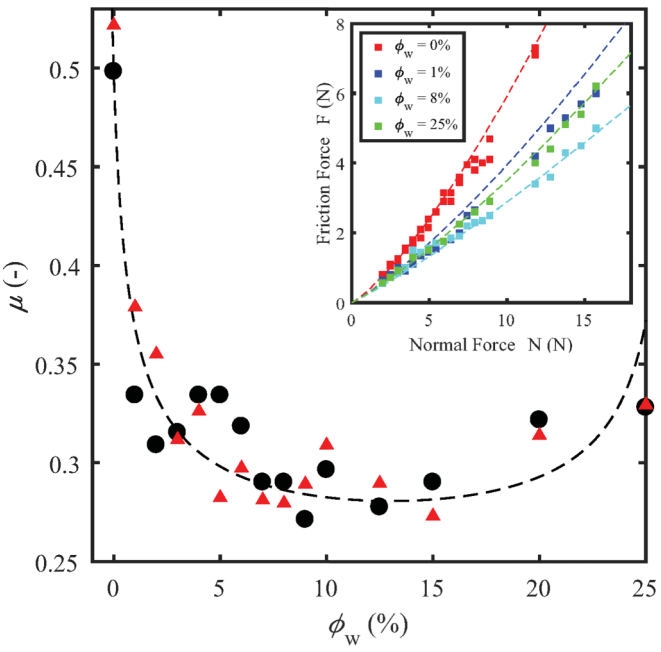

FIG. 2. Evolution of the friction coefficient μ for the water volume fraction ϕ_w. The friction coefficient obtained from the measured friction force and fixed normal force ($N = 7.9$ N) in black circles display a nonmonotonic behavior for increasing water fraction. With use of the ploughing model, the friction coefficient can be modeled either based on the ploughing track radius r [Eq. (2), red triangles] or based on the penetration hardness P_h of the water-sand mixture [Eq. (3), dashed line]. The inset shows the friction force as a function of the normal force for various water volume fractions experimentally (squares) and predicted by the ploughing model based on the penetration hardness P_h (dashed line).

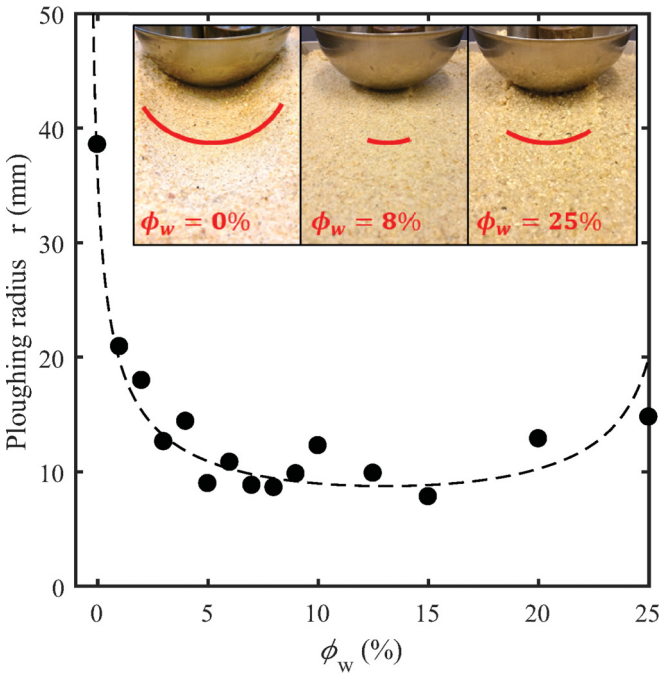

FIG. 3. Ploughing radius r as a function of water volume fraction ϕ_w for a fixed normal force of $N = 7.9$ N. Like the friction coefficient, the ploughing track width (black circles) evolves nonmonotonically with the water content, also shown based on the ploughing model (dashed line, $r = \sqrt{\frac{N}{\frac{1}{2}\pi P_h(\phi_w)}}$). The inset shows images of the experiments for $\phi_w = 0\%$, 8%, and 25% with red lines highlighting the ploughing tracks.

The ploughing motion of the hemisphere involves an analogous deformation in the tangential direction.

We now use a well-known method introduced for metal-on-metal ploughing [22,23] to calculate the ploughing force. Ploughing starts if the tangential pressure on the water-sand mixture exceeds its penetration hardness P_h; therefore, the ploughing force can be written in terms of the penetration hardness and the cross sectional area as $F_P = P_h A_P$ with $A_P = \frac{2r^3}{3R}$ [see Fig. 1(b)]. Subsequently, the friction coefficient is the ratio of the ploughing force to the normal force

$$\mu = \frac{P_h A_P}{N} + \mu_0. \tag{1}$$

To account for the fact that even in the absence of ploughing a frictional force will resist the sliding, we introduce μ_0 as the surface friction contribution. Using the definition of the penetration hardness and Eq. (1), the friction coefficient μ can now be expressed in terms of the ploughing track size as

$$\mu = \frac{4r(\phi_w, N)}{3\pi R} + \mu_0. \tag{2}$$

Equation (2) indeed suggests that the deeper the hemisphere ploughs into the sand, the larger the friction is, as observed in Figs. 2 and 3. Furthermore, from Eq. (2) we can now calculate the friction coefficient using the imposed normal force N, the measured track width r, and the surface friction contribution μ_0. Indeed, the calculated friction coefficient is in good agreement with the measured friction coefficient (black circles and red triangles in Fig. 2).

Alternatively, the friction coefficient can be expressed in terms of the penetration hardness P_h, the imposed normal force N, and the surface friction coefficient μ_0:

$$\mu = \frac{4\sqrt{2}}{3\pi^{3/2}R}\sqrt{\frac{N}{P_h(\phi_w)}} + \mu_0. \tag{3}$$

In Fig. 2 we plot this function (dashed line) using the relation between penetration hardness and water content obtained for normal forces ranging from 2.5 to 16 N in Fig. 4. Again, we find good agreement between the ploughing model and the experiment. Finally, Eq. (3) explicitly predicts a superlinear increase of the friction force F as a function of the normal force: $F \sim N^{3/2} + \mu_0 N$. We indeed observe such behavior for different water-sand mixtures (inset Fig. 2); also note that the nonmonotonic behavior of the friction force for increasing water content is sustained over the full range of imposed normal forces probed here.

The only adjustable parameter in the ploughing model is the surface friction contribution $\mu_0 = 0.21$ corresponding to the sliding friction between the hemisphere and the sand grains. When there is no permanent deformation of the water-sand packing, we expect the total friction to be equal to μ_0, $\mu = \mu_0$, corresponding to $R = 0$ in Eq. (2). To obtain exactly this type of sliding motion, we now fix a collection of sand grains to a plate using glue. The hemisphere is then pulled over these immobilized sand grains using normal forces

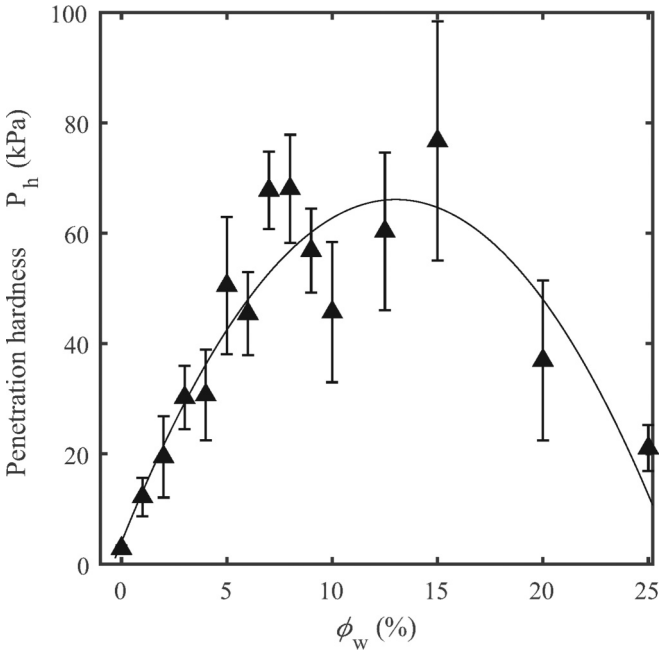

FIG. 4. Penetration hardness P_h as a function of water volume fraction ϕ_w. The contact pressure $P_h = N/A_c$, where the projected contact area $A_c = \frac{1}{2}\pi r^2$ is obtained from the ploughing track radius r. With use of varying dead weight, the normal force is varied from 2.5 up to 16 N for each water-sand mixture and subsequently the track radius is measured, which enables one to calculate an average penetration hardness. The error bars represent the standard deviation. The solid line describes the data based on a first-order increase due to liquid bridge formation and an exponential decrease based on the coalescence of these liquid bridges.

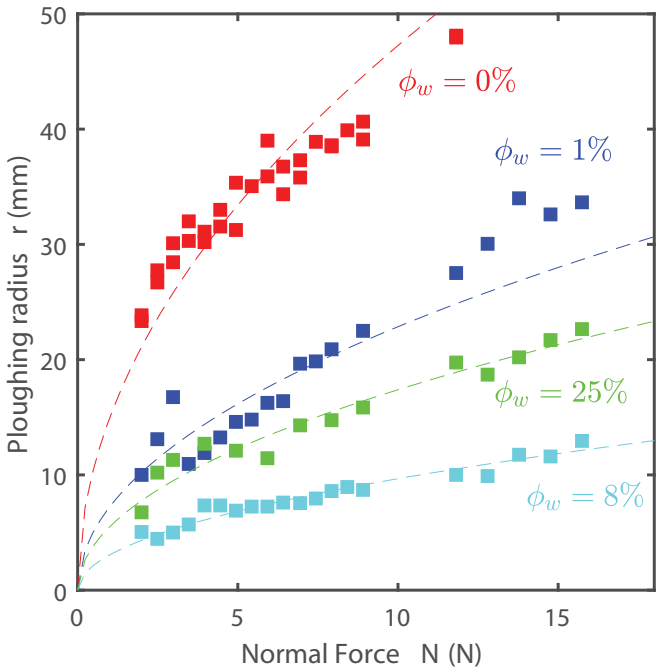

FIG. 5. Ploughing radius r as a function of normal force N for various water volume fractions. The squares represents the experimental data and the dashed lines reflects the model ($r = \sqrt{\frac{N}{\frac{1}{5}\pi P_h(\phi_w)}}$) based on the penetration hardness. The radius increases with the normal force and has a minimum for $\phi_w = 8\%$. Note that the nonmonotonic behavior of the track radius for increasing water content holds over the full domain of normal forces.

ranging from 2.5 up to 16 N. The measured friction coefficient $\mu_0 = 0.19 \pm 0.09$ is in good agreement with the value that was used to match the ploughing model to the experimental data in Fig. 2: $\mu_0 = 0.21$.

Earlier experiments found a relation between the adhesive forces between sand grains and the relative humidity [24,25]. We expect this effect not to be important here because the adsorption of water on dry sand grains is relatively small as long as the ambient relative humidity is below 60%, which it is in our laboratory. Therefore, the grain-grain adhesive force, mainly based on the capillary pressure, will have a minor influence on the ploughing experiment for dry sand.

III. DISCUSSION

The effect of the nonmonotonic behavior of the hardness of granular materials for increasing water fraction is not restricted to sliding in a simple sphere-on-flat geometry. For example, the impact cratering of a sphere in a granular material depends strongly on the water fraction. Marston *et al.* [26] present experimental results for the penetration of a solid sphere when released on a granular material. The minimum penetration depth of the object (corresponding to a zero-impact speed) and yield stress of the granular material reveal qualitatively similar nonmonotonic behavior as a function of increasing water fraction compared to that found here for the width of the ploughing track and the penetration hardness. Consequently, the nonmonotonic variation of the hardness with increasing water content will also impact the friction behavior when geometries other than a sphere-on-flat one are used.

The nontrivial relation between the friction coefficient and the water content of a granular material can therefore be understood in terms of the stiffness (penetration hardness) of the granular material. Fall *et al.* [19] have shown previously that the friction coefficient decreases roughly linearly with the increase in the elastic shear modulus; qualitatively this makes sense as one expects the penetration hardness and the (linear) shear modulus to be strongly correlated: If the critical strain which defines the transition from elastic to plastic deformation is independent of the water volume fraction, the elastic shear modulus and penetration hardness are proportional. The sphere-on-flat geometry used here, however, allows us to obtain a quantitative relation between the friction coefficient and the penetration hardness as $\mu \sim P_h^{-1/2}$. This is difficult for the sledges used in the experiment by Fall *et al.* [19] because the penetration of the sledge is harder to quantify.

The ploughing friction quantified here is not specific for granular materials as ploughing is a typical form of wear that is generically encountered when one of the two materials

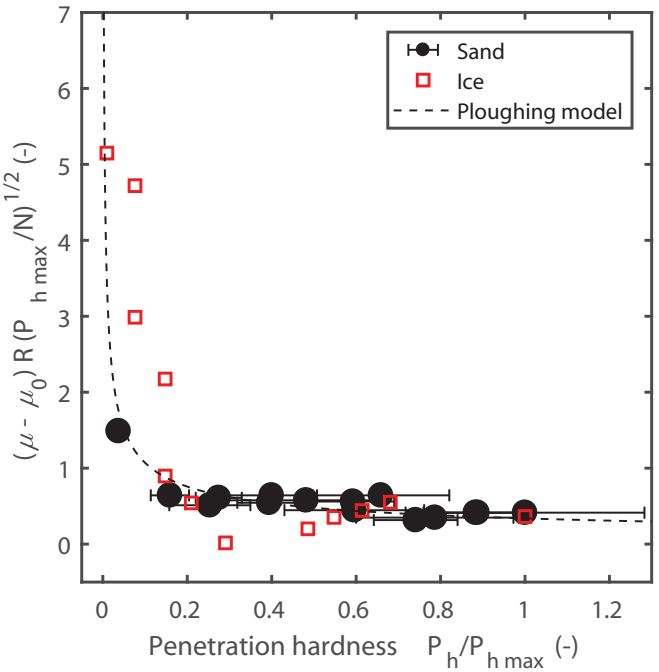

FIG. 6. Master curve which shows the collapse of ploughing through sand and ice (data from [27]) when the ploughing friction is plotted versus the relative penetration hardness with use of rescaling based on the ploughing model (3). The friction coefficient for ploughing through sand is given for $P_{h\,max} = 76.7$ kPa and $N = 7.9$ N. Weber *et al.* [27] obtained the steel-on-ice friction coefficient as a function of temperature, where the penetration hardness decreases linearly with increasing temperature. The high-temperature regime ($T = [-21, 0]\,^\circ$C), where the plastic ploughing dominates, is replotted with use of the sphere radius $R = 2.38$ mm, the normal force $N = 1$ N, the maximum penetration hardness $P_{h\,max} = 233.1$ MPa, and a surface friction contribution of $\mu_0 = 0.01$.

is much harder than the other. In metal-metal systems, the increase of friction with penetration depth is well known [22,23]. Friction on ice, for instance, depending on the conditions, can be dominated by ploughing. In particular, it has been shown that close to the melting point of ice, the penetration hardness controls the friction force [27]. The ice penetration hardness decreases roughly linearly for temperatures approaching 0 °C [28], resulting in an increase of the friction coefficient from the very low friction coefficients typical for ice skating (0.03) to much higher ones, comparable to the surface friction coefficient found here (0.17 for the ice skating). Our simple ploughing model also captures the evolution of the metal-on-ice friction presented in Ref. [27]; in Fig. 6 we collapse the friction force observed in both systems onto a single master curve by rescaling with use of the ploughing model (3), demonstrating that the same model applies in completely different systems.

IV. CONCLUSION

We have presented sliding experiments of a hemisphere on wetted sand in which we imposed the normal force and measured the pull force and the width of the ploughing track. For a given normal force, both the pulling force and the width of the ploughing track show a minimum for a water volume fraction of around 10%, where the measured penetration hardness of the water-sand mixture is maximal. This behavior is fully consistent with the ploughing model in which the sphere-on-flat geometry is exploited to express the friction coefficient as a function of the normal force and penetration hardness (or ploughing track radius).

ACKNOWLEDGMENT

We thank Daan Haver for help with the experiments and Shell for financial support (PT 67354).

[1] A. G. Bengough, B. McKenzie, P. Hallett, and T. Valentine, J. Exp. Bot. **62**, 59 (2011).
[2] A. Abdalla, D. Hettiaratchi, and A. Reece, J. Agric. Eng. Res. **14**, 236 (1969).
[3] B. D. Texier, A. Ibarra, and F. Melo, PLoS ONE **12**, e0175412 (2017).
[4] C. Li, T. Zhang, and D. I. Goldman, Science **339**, 1408 (2013).
[5] D. Griffiths, J. Anim. Ecol. **49**, 99 (1980).
[6] J. Crassous, A. Humeau, S. Boury, and J. Casas, Phys. Rev. Lett. **119**, 058003 (2017).
[7] J. P. Hambleton, S. Stanier, D. J. White, and S. W. Sloan, Aust. Geomech. J. **49**, 147 (2014).
[8] F. J. Muzzio, T. Shinbrot, and B. J. Glasser, Powder Technol. **124**, 1 (2002).
[9] V. Matousek, Exp. Therm. Fluid Sci. **26**, 693 (2002).
[10] J. Duran, *Sands, Powders, and Grains: An Introduction to the Physics of Granular Materials* (Springer, New York, 2000).
[11] N. Mitarai and F. Nori, Adv. Phys. **55**, 1 (2006).
[12] M. Badetti, A. Fall, F. Chevoir, and J.-N. Roux, Eur. Phys. J. E **41**, 68 (2018).
[13] K. M. Frye and C. Marone, J. Geophys. Res. **107**, ETG 11-1 (2002).
[14] O. Dorostkar, R. A. Guyer, P. A. Johnson, C. Marone, and J. Carmeliet, J. Geophys. Res. **123**, 2115 (2018).
[15] L. Kovalcinova, S. Karmakar, M. Schaber, A.-L. Schuhmacher, M. Scheel, M. DiMichiel, M. Brinkmann, R. Seemann, and L. Kondic, Phys. Rev. E **98**, 032905 (2018).
[16] J. Duriez, M. Eghbalian, R. Wan, and F. Darve, J. Mech. Phys. Solids **99**, 495 (2017).
[17] P. C. Møller and D. Bonn, Europhys. Lett. **80**, 38002 (2007).
[18] M. Pakpour, M. Habibi, P. Møller, and D. Bonn, Sci. Rep. **2**, 549 (2012).
[19] A. Fall, B. Weber, M. Pakpour, N. Lenoir, N. Shahidzadeh, J. Fiscina, C. Wagner, and D. Bonn, Phys. Rev. Lett. **112**, 175502 (2014).
[20] P. E. Newberry, *El Bersheh: The Tomb of Tehuti-Hetep* (Egypt Exploration Fund, London, 1895), Vol. 1.
[21] S. Ayrinhac, Tribol. Online **11**, 466 (2016).
[22] F. Bowden, A. Moore, and D. Tabor, J. Appl. Phys. **14**, 80 (1943).
[23] R. Spurr, Br. J. Appl. Phys. **7**, 260 (1956).
[24] M. Bazrafshan, M. de Rooij, and D. Schipper, Int. J. Mech. Sci. **140**, 471 (2018).
[25] D. B. Asay and S. H. Kim, J. Phys. Chem. B **109**, 16760 (2005).
[26] J. O. Marston, I. U. Vakarelski, and S. T. Thoroddsen, Phys. Rev. E **86**, 020301(R) (2012).
[27] B. Weber, T. Suhina, T. Junge, L. Pastewka, A. Brouwer, and D. Bonn, Nat. Commun. **9**, 888 (2018).
[28] P. Barnes and D. Tabor, Plastic flow and pressure melting in the deformation of ice, Ph.D. thesis, University of Cambridge, 1969.